



Effect of Co Content on the Microstructure and Corrosion Behavior of $\text{Al}_{0.3}\text{Co}_x\text{CrFeNi}$ High Entropy Alloys

Zequn Zhang¹ · Qijuan Dong¹ · Zhibin Chen¹ · Junsheng Wu^{1,2} · Jiuyang Xia¹ · Kang Huang¹ · Pengcheng Zuo¹ · Wei Xue¹ · Bowei Zhang^{1,2}

Received: 22 February 2023 / Accepted: 25 July 2023 / Published online: 29 August 2023
© The Author(s) under exclusive licence to The Korean Institute of Metals and Materials 2023

Abstract

The influence of Co content on the microstructure and corrosion behavior of $\text{Al}_{0.3}\text{Co}_x\text{CrFeNi}$ ($x=0.25, 0.5$ and 1.0) high entropy alloys were investigated. The results indicated that the increased content of Co improve the corrosion resistance of alloy, which can be attributed to the distinction of phase composition in alloys caused by different Co content. The $\text{Al}_{0.3}\text{Co}_x\text{CrFeNi}$ alloy shows a double-phase (FCC+BCC) structure for $x=0.25$ and 0.5 , and BCC phase consists of (Al, Ni)-rich B2 phase and (Cr, Fe, Co)-rich A2 phase. The increase of Co content induces the transformations of crystal-structures from BCC to FCC, resulting in the decrease of BCC phase proportion. The $\text{Al}_{0.3}\text{CoCrFeNi}$ alloy exhibits the single FCC structure, and all elements tend to be homogeneously distributed. The difference in the potential of FCC and BCC phases indicates the BCC phase acts as anode resulting to localized corrosion, while B2 phase preferentially dissolves compared to the A2 phase due to the lower potential. Therefore, the existence of selective corrosion is found in the alloys with double-phase, by contrast, the alloy with single FCC phase shows random pitting corrosion.

Keywords High entropy alloys · Co content · Microstructure · Corrosion behavior

1 Introduction

As a novel design idea of alloys that breaks the traditional alloy design concept, the high-entropy alloys (HEAs) have attracted extensive attentions of researchers in recent years [1, 2]. Specifically, HEA is defined as alloy containing five or more principal elements with an equal or near-equal atomic ratio, which provides considerable freedom for the design of new materials [3, 4]. The composition of multi-principal element makes HEAs possess four core effects, which consist of the high-entropy effect, the lattice distortion effect, the sluggish diffusion effect, and the cocktail effect [2, 5]. Generally, HEAs are prone to form solid solutions with face-centred cubic (FCC), body-centered cubic

(BCC) or hexagonal closed-pack (HCP) structures rather than complex intermetallic compounds due to the high mixing entropy effect [1, 5]. Compared to the traditional alloys, HEAs have exhibited multiple performances, including high strength-ductility combination, good structural stability, outstanding wear resistance, etc. [6–10]. The simple structure and excellent properties make that HEAs are endowed with promising prospect of industrial and engineering applications, such as infrastructure, military equipment, aerospace industries and functional coatings [2, 11].

In order to fulfill the demands of different engineering environments, the corrosion resistance of HEAs is an important index, which should be entirely considered. Based on recent research [5, 12, 13], HEAs have shown better corrosion resistance than traditional corrosion-resistant alloys, e.g., stainless steels and Ni-based alloys. The compositions of HEAs contain high contents of passivation elements (Cr, Ni, Al, Mo, etc.), resulting in the formation of passive films on surface, which well explains the superior corrosion resistance of HEAs [14, 15]. For example, the stable Cr species significantly contribute to the compactness and protective of the passive films [16, 17]. On the other hand, the microstructure and phase compositions of HEAs also act as the

✉ Bowei Zhang
bwzhang@ustb.edu.cn

¹ Institute for Advanced Materials and Technology, University of Science and Technology Beijing, Beijing 100083, China

² National Materials Corrosion and Protection Data Center, University of Science and Technology Beijing, Beijing 100083, China

crucial role of their corrosion behavior. It has been reported that the HEAs with duplex FCC + BCC structure possesses selective corrosion behavior of different phases, showing the (Al, Ni)-rich BCC phase is prone to preferentially dissolve [18–20]. In addition, the corrosion resistance of HEAs is also influenced by the grain size [21], dislocation density [22], etc. It is worthwhile to further analyze the factors affecting corrosion resistance and establish the corrosion mechanism for enlarging the potential applications of the HEAs.

To date, the microstructure and properties of HEAs about AlCoCrFeNi-based system were widely studied [19, 23]. Numerous researchers have reported that the changes in chemical composition of HEAs could result in the regulation of microstructure and improvement of properties [24–26]. It is very common to directly adjust the content of a certain element. Yang et al. [27] demonstrated that the increase of Al content in $\text{Al}_x\text{CoCrFeNi}$ HEAs ($x = 0.3, 0.5, 0.7$) encourages the transformation from FCC phase to BCC phase, which degrades the localized corrosion resistance. Zhang et al. [28] investigated the influence of Ni content on the corrosion evolution of $\text{Al}_{0.5}\text{CoCrFeNi}_x$ HEAs. The result indicated that the selective dissolution replaces the uniform corrosion with the Ni content increase due to the formation of (Al, Ni)-rich B2 phase with weak stability. Similar studies about adjustment of composition content are very abundant, but it is worth noting that the reports focused on the changes of HEAs caused by Co content are relatively uncommon. Co element has been proven to promote the formation of FCC phase in Al-Co-Cr-Fe-Ni HEA system, and the increase concentration of Co deteriorate the strength but improve the ductility of the HEA [29, 30]. Additionally, the existence of Co species in passive film of HEA is beneficial for the enhancement of the corrosion resistance [16, 31]. However, there is a lack of investigation on the variation of corrosion behavior by adjust the Co content in HEAs. It is necessary to further explore the influence of Co content on microstructure and corrosion behavior of HEAs.

In this paper, the present work focused on the microstructure and corrosion behavior of the $\text{Al}_{0.3}\text{Co}_x\text{CrFeNi}$ ($x = 0.25, 0.5$ and 1.0) HEAs. Based on the microstructure characterizations and corrosion tests, we investigated the influences of Co content on $\text{Al}_{0.3}\text{Co}_x\text{CrFeNi}$ HEAs and established the relationships between microstructure and corrosion behavior. The results deepen the fundamental understanding of localized corrosion mechanism of HEAs and provide the

reference suggestions for practical application and future design of HEAs.

2 Materials and Methods

The nonequimolar $\text{Al}_{0.3}\text{Co}_x\text{CrFeNi}$ HEAs ($x = 0.25, 0.5$ and 1.0) were prepared by arc-melting with the mixtures of the pure metal (Al, Fe, Cr, Co and Ni) with purities up to 99.99% in an argon atmosphere. The ingots were remelted times to ensure its homogeneity. The chemical homogeneity of ingot composition was ensured by remelting alloys at least five times. Table 1 lists the chemical compositions of the different alloys, which are consistent with nominal composition. The alloys with different Co content are hereafter denoted by $\text{Co}_{0.25}$, $\text{Co}_{0.5}$ and $\text{Co}_{1.0}$ alloys. The samples were cut into the size of $10 \text{ mm} \times 10 \text{ mm} \times 3 \text{ mm}$ and then the specimens were grinded, polished and cleaned for subsequent experiments.

Phase identification of $\text{Al}_{0.3}\text{Co}_x\text{CrFeNi}$ HEAs was carried out by X-ray diffraction (XRD, D8Advance). The microstructures of the different samples were investigated by scanning electron microscope (SEM, Regulus8100) equipped with energy-dispersive spectrum (EDS). The electron backscattered diffraction (EBSD) tests were performed using the Tescan Mira 3 LMH scanning electron microscope and the results were analyzed with the Channel5 software. The transmission electron microscope (TEM, TECNAI F20) analysis were undertaken to obtain the selected area electron diffraction (SAED) patterns, scanning transmission electron microscopy (STEM) images and energy-dispersive X-ray spectroscopy (EDXS) maps.

The scanning kelvin probe force microscopy (SKPFM) measurement was conducted with Atomic Force Microscopy (MultiMode 8, Bruker) in the PeakForce Tapping mode. Specifically, The PFQNE-AL probes with a force constant of 0.8 N/m and a resonance frequency of 300 kHz were utilized in SKPFM measurements. In order to obtain the second signal in addition to the surface topographic signal, the measurements were conducted in dual-scan mode. During the KPFM measurement, once there is a potential difference between the tip and the sample, an AC voltage is applied to the tip to induce harmonic oscillation of the cantilever. Subsequently, the tip is subjected to a voltage of equal magnitude to stop the oscillation and reduce the potential difference. The work function derived with this method is closely associated with the corrosion potential, and the lower work function of material usually indicates the lower potential and higher susceptibility to corrosion [32, 33].

The electrochemical measurements were conducted using an PGSTAT302 N Autolab electrochemical workstation in 3.5 wt% NaCl solution at room temperature. The

Table 1 Chemical compositions of as-cast $\text{Al}_{0.3}\text{Co}_x\text{CrFeNi}$ alloys (at%)

Alloys	Al	Co	Cr	Fe	Ni
$\text{Co}_{0.25}$	8.46	7.04	28.17	28.16	28.17
$\text{Co}_{0.50}$	8.30	12.82	25.63	25.63	27.63
$\text{Co}_{1.0}$	6.96	23.22	23.25	23.26	23.31

conventional three-electrode system for tests consisted of a platinum sheet as the counter electrode, a saturated calomel electrode (SCE) reference electrode, and the specimen with an exposed area of 1 cm^2 acting as the working electrode. The potentiodynamic polarization curves and electrochemical impedance spectroscopy (EIS) tests were measured after obtaining a stable open circuit potential (OCP). The potentiodynamic polarization curves were scanned from -0.5 V (vs. E_{ocp}) to -1.5 V (vs. E_{SCE}) with a scan rate of 1 mV/s and the EIS tests were carried out at the OCP in the ranges from 100 kHz to 10 mHz with a sinusoidal potential amplitude of 10 mV . The results of polarization curves were analyzed by Nova software and EIS data were fitted using ZsimpWin software. All experiments were repeated more than three times under the same condition to ensure data reproducibility.

3 Results and Discussion

Figure 1 shows the typical XRD spectras of the $\text{Al}_{0.3}\text{Co}_x\text{CrFeNi}$ alloy. Diffraction peaks corresponding to the face-centered cubic (FCC) and body-centered cubic (BCC) phase are generally identified for the $\text{Co}_{0.25}$ alloy. The intense peaks indicating BCC structure are observed and the peak of (100) plane confirms the existence of B2 phase [34]. The incorporation of more Co effectively stabilizes the FCC structure due to the improvement of valance electron concentration (VEC) that determine the crystallographic lattice (FCC or BCC) and structure stability [29, 30,

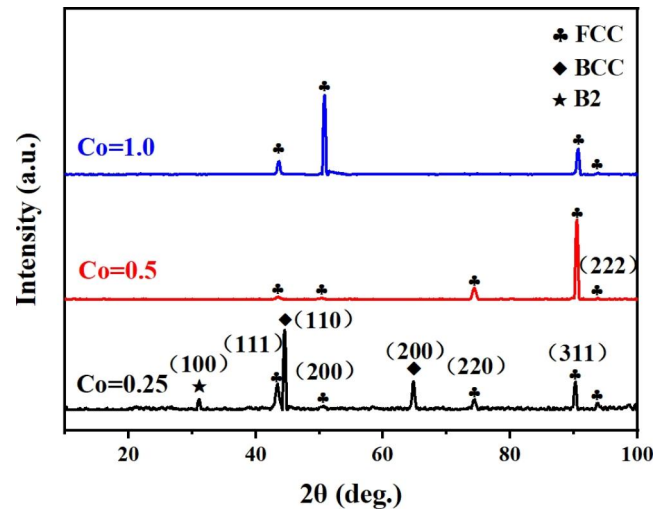


Fig. 1 The XRD patterns of $\text{Al}_{0.3}\text{Co}_x\text{CrFeNi}$ ($x=0.25, 0.5,$ and 1.0) alloys

35]. With the content of Co increasing, XRD patterns reveal the principal phases transform process from BCC to FCC. So the diffraction peaks of the BCC phase almost disappear and the peaks of the FCC structure are still displayed in the $\text{Co}_{0.5}$ and $\text{Co}_{1.0}$ alloys. The XRD results indicate that Co element promotes the formation of FCC phase.

The EBSD results and SEM images showing the microstructures of $\text{Al}_{0.3}\text{Co}_x\text{CrFeNi}$ alloys with different Co contents are presented in Fig. 2. As shown in Fig. 2a, d and g, it is clearly demonstrated that the grains display random orientations and characteristics of large-sized columnar grain in all alloys. The FCC and BCC phases of the $\text{Al}_{0.3}\text{Co}_x\text{CrFeNi}$

Fig. 2 IPF images, phase maps and SEM images of the $\text{Al}_{0.3}\text{Co}_x\text{CrFeNi}$ HEA: (a–c) $\text{Co}_{0.25}$, (d–f) $\text{Co}_{0.5}$ and (g–i) $\text{Co}_{1.0}$

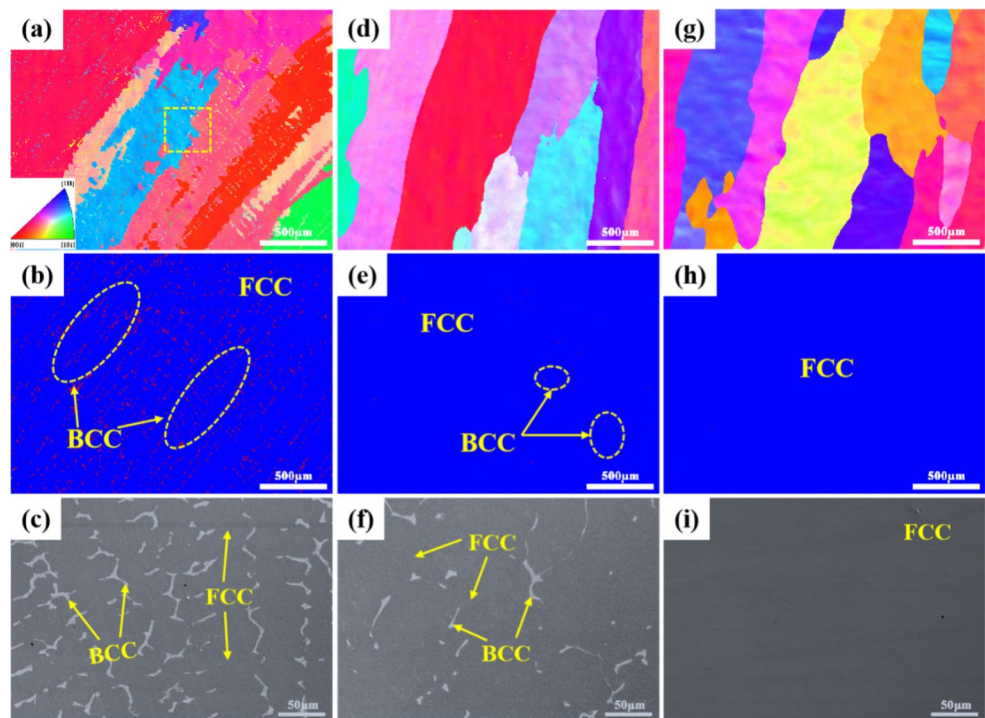


Fig. 3 SEM images and corresponding EDS mappings of the $\text{Al}_{0.3}\text{Co}_x\text{CrFeNi}$ HEA: (a, b) $\text{Co}_{0.25}$, (c) $\text{Co}_{0.5}$ and (d) $\text{Co}_{1.0}$

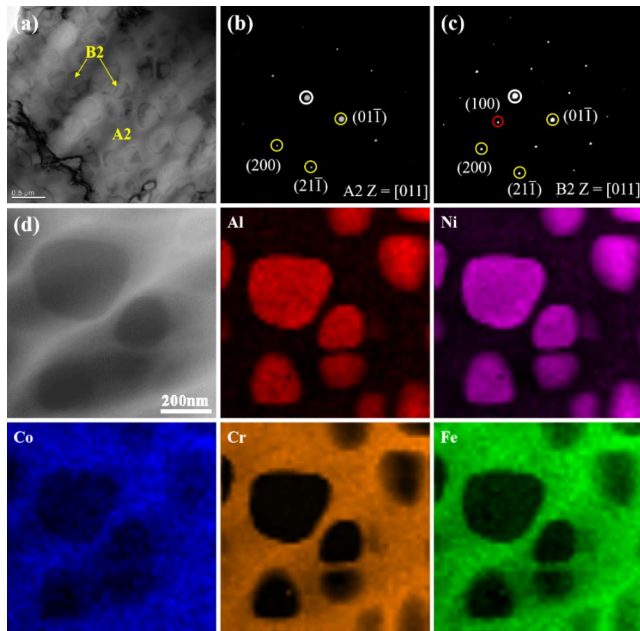
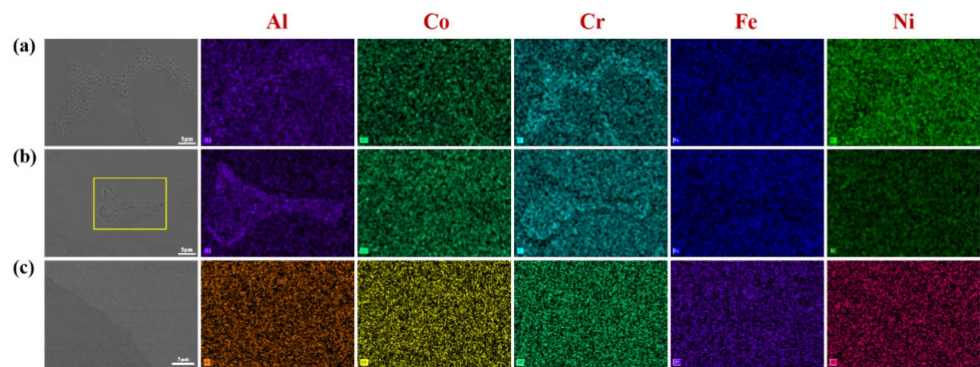


Fig. 4 Results of TEM analysis for the B2 phase and A2 phase of the $\text{Co}_{0.25}$ alloy: (a) STEM image, (b, c) SAED diagrams and (d) STEM image and corresponding STEM-EDS maps

alloys are labeled as blue and red colors in the phase maps of the EBSD results, respectively (Fig. 3d, e and h). Two-phase microstructure exists in the $\text{Co}_{0.25}$ and $\text{Co}_{0.5}$ alloys, but the proportion of BCC phase decreases dramatically with the further increased Co content. The absence of BCC phase diffraction peaks in the XRD pattern of the $\text{Co}_{0.5}$ alloy can be explained by the limited fraction of BCC phase. The $\text{Co}_{1.0}$ alloy is confirmed to possess single FCC phase structure. Figure 2c and f reveal the obvious dendritic and inter-dendritic structures in $\text{Co}_{0.25}$ and $\text{Co}_{0.5}$ alloys, and the dendritic regions consist of FCC phase whereas interdendritic regions consist of BCC phase combining the phase maps in Fig. 2 [30, 36]. With increasing the Co content in the alloys, the interdendritic regions is significantly reduce, implying the decrease in the amount of the BCC phase. In contrast, no clear dendritic structure is observed in $\text{Co}_{1.0}$ alloy (Fig. 2i), indicating the formation of single FCC phase.

Figure 3 exhibits the SEM images and corresponding EDS results of $\text{Al}_{0.3}\text{Co}_x\text{CrFeNi}$ alloys. For the $\text{Co}_{1.0}$ alloy with the single FCC structure, all constituent elements are distributed homogeneously in the FCC solid solution (Fig. 3c). As shown in Fig. 3a and b, the interdendritic regions with BCC structure are enriched in Al and Cr and other elements show insignificant enrichment, whereas the dendritic regions poor in Al and Cr form FCC structure. Similar phenomena have reported in the previous literatures [29, 30]. Two distinct morphologies can be seen in the BCC phase by focusing on the interdendritic regions. The net-like phase and dense nano-sized particles are distributed in the inter-dendritic regions, and there are differences between them in composition due to obvious changes in contrast of the SEM images.

In order to further analyze the structure and elements distributions of the BCC phase, the in-depth observation of $\text{Co}_{0.25}$ alloy was conducted by TEM (Fig. 4). The microstructure of BCC phase consists of two alternating bright and dark regions, corresponding to the net-like phase and dense nano-sized particles, respectively. Both phases possess similar structure, the SAED pattern of net-like phase along the [001] zone axis (Fig. 4b) is consistent with the presence of disordered A2 phase, and the existence of ordered B2 phase indicates by the SAED pattern (Fig. 4c) along the [001] zone axis [37, 38]. The distinction of both SAED patterns is indicated by the (100) super-lattice spot exclusive to the ordered BCC phase [14]. Combined with the STEM image and corresponding STEM-EDS maps (Fig. 4c), the regions where nano-sized particles (B2 phase) existed rich in Al and Ni, whereas the net-like A2 matrix (A2 phase) next to the particles are enriched in Cr, Fe and Co. Due to the relatively larger negative mixing enthalpy of Al and Ni than the other atomic pair in the alloy system, the Al and Ni elements are repulsed by Fe, Cr, Co elements and inclined to aggregating at certain regions, and form (Al, Ni)-enriched phase lacking other elements [20, 34].

Figure 5 presents the polarization curves for the HEAs with different Co content in the 3.5 wt% NaCl solution at room temperature. Typical active-passive transition regions

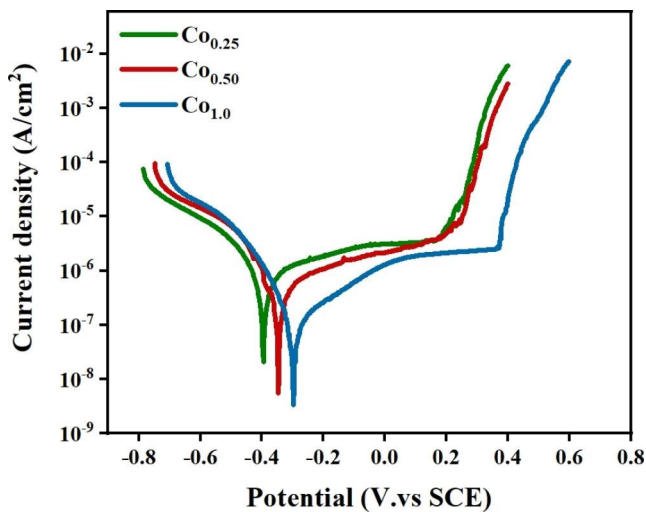


Fig. 5 Potentiodynamic polarization curves of the $\text{Al}_{0.3}\text{Co}_x\text{CrFeNi}$ ($x=0.25, 0.5,$ and 1.0) alloys in 3.5 wt% NaCl solution

Table 2 Fitting results of polarization curves for $\text{Al}_{0.3}\text{Co}_x\text{CrFeNi}$ ($x=0.25, 0.5,$ and 1.0) alloys

Alloys	E_{corr} (mV)	I_{corr} ($\mu\text{A}/\text{cm}^2$)	E_{pit} (mV)
Co0.25	-396	1.06	166
Co0.50	-348	0.45	187
Co1.0	-298	0.18	372

are not found and the obvious passive regions are existed in all curves, indicating the passive films could form spontaneously in the solution [39]. Furthermore, the passive region of $\text{Co}_{1.0}$ alloy is significantly broader than that of $\text{Co}_{0.25}$ and $\text{Co}_{0.5}$ alloys. The electrochemical parameters obtained from polarization curves are given in Table 2. In general, the alloy with higher corrosion potential (E_{corr}), lower corrosion current density (i_{corr}) and larger pitting potential (E_{pit}) reveals

more excellent corrosion resistance [40]. With the increase of Co content in HEA, the i_{corr} decreases and E_{corr} increases, suggesting the resistance of general corrosion strengthen. In addition, the $\text{Co}_{1.0}$ alloy possesses more stable protective film and higher pitting resistance due to the broader potential range of the passive process and the higher value of E_{pit} . Thus it is reasonable to consider a better corrosion resistance for the $\text{Co}_{1.0}$ alloy compared to the $\text{Co}_{0.25}$ and $\text{Co}_{0.5}$ alloys.

Figure 6 shows the EIS results of different HEAs in the 3.5 wt% NaCl solution at OCP. As shown in Fig. 6a, the Nyquist plots of all HEAs displays as capacitive semicircles arcs, indicating similar electrochemical corrosion behavior of the three alloys. The diameters of the capacitive semicircles increase with the improvement of Co content, implying the enhancement of corrosion resistance. As for the Bode plots in Fig. 6b, the existence of the solution resistance (pure resistor) in the high frequency range is identified due to the impedance modulus keeps constant low value and the phase angles are close to zero [16]. In the medium and low frequencies ranges, the linear relationships between $\log|Z|$ and $\log f$ are displayed and the phase angles reach maximum values for each plot, which can be attributed to capacitive-like characteristics of passive film [15, 23]. Moreover, the $|Z|$ values of the $\text{Co}_{1.0}$ alloy is the highest among the alloys, which illustrates the $\text{Co}_{1.0}$ alloy exhibits the best corrosion resistance among the HEAs. The equivalent electrical circuit inserted in Fig. 6a is used to fitting the results of EIS and the related parameters are summarized in Table 3. In the circuit [39], R_s represents the solution resistance, Q_f indicates the constant phase element (CPE) associated with the capacitance of the passive film, R_f stands for the resistance of the film, Q_{dl} represents the CPE related to the interfacial electric double layer, and R_{ct} is the charge transfer resistance.

Fig. 6 EIS measurements of the $\text{Al}_{0.3}\text{Co}_x\text{CrFeNi}$ ($x=0.25, 0.5,$ and 1.0) alloys in 3.5 wt% NaCl solution: (a) Nyquist plots and equivalent circuit model; (b) Bode plots

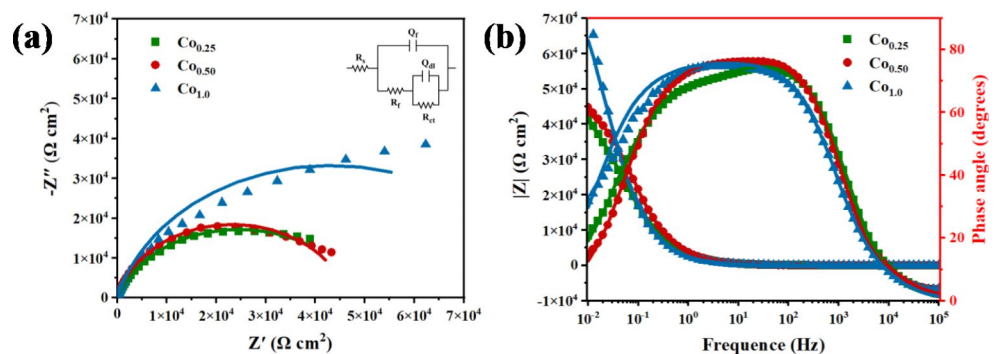


Table 3 The fitting parameters of EIS measurements for $\text{Al}_{0.3}\text{Co}_x\text{CrFeNi}$ ($x=0.25, 0.5,$ and 1.0) alloys

Alloys	R_s ($\Omega \text{ cm}^2$)	Q_f ($\Omega^{-1} \text{ cm}^{-2} \text{ s}^n$)	n_f	R_f ($\Omega \text{ cm}^2$)	Q_{dl} ($\Omega^{-1} \text{ cm}^{-2} \text{ s}^n$)	n_{dl}	R_{ct} ($\Omega \text{ cm}^2$)
$\text{Co}_{0.25}$	6.68	4.95×10^{-5}	0.80	2.82	2.88×10^{-5}	0.80	4.76×10^4
$\text{Co}_{0.50}$	6.84	4.92×10^{-5}	0.84	4.56	6.34×10^{-6}	1.00	4.68×10^4
$\text{Co}_{1.0}$	6.85	2.21×10^{-5}	0.93	3.89	5.95×10^{-5}	0.80	8.68×10^4

With the increase of Co content, the value of R_f and R_{ct} show a trend of gradual increasing, which also indicates the improvement of corrosion resistance. In conclusion, the comparison of EIS measurements between different HEAs suggests the $Co_{1.0}$ alloy possesses most superior corrosion resistance and the $Co_{0.25}$ alloy exhibits the worst corrosion resistance, which is in accord with the experiment results of polarization tests.

In order to intuitively reflect the corrosion behavior of different alloys, the corrosion morphologies of HEAs after potentiodynamic polarization are examined by SEM. The results show that the obvious localized corrosion exists in all specimens and the corrosion regions with size about $300\ \mu\text{m}$ are illustrated on the surface. As shown in Fig. 7a–c, the deep pit left by dissolution of BCC phase and the appearance of nanoscale porous structure of BCC phase confirm the selective corrosion of the BCC phase in $Co_{0.25}$ alloy, which indicates that the FCC phase is more difficult to suffer the attack of Cl^- compared to the BCC phase. Some cubic grooves formed by preferential dissolution of B2 phase in BCC matrix can be easily distinguished and the net-like A2 phase exhibits better corrosion resistance due to the relatively smooth surface. Therefore, the selective corrosion is the dominant corrosion behavior of $Co_{0.25}$ alloy ascribed to the complication of the phase components. Except for selective corrosion of BCC phase, obvious pitting corrosion can be observed in the $Co_{0.5}$ alloy, which can be attributed to the decrease of content of BCC phase (Fig. 7d–f). In addition, the phenomenon of preferential dissolution of B2 phase also exist. As for the $Co_{1.0}$ alloy (Fig. 7g–i), apart from the existence of several obvious and larger-sized corrosion pits, a

lot of small corrosion pits with size about $1\ \mu\text{m}$ are also observed on the surface. All pits of pitting corrosion tend to be randomly distributed on the single FCC-phase sample. Overall, the results shown in Fig. 7 indicate that the localized corrosion mechanism of the $Al_{0.3}Co_xCrFeNi$ alloy change from selective corrosion to pitting corrosion as the content of Co increases.

The nano-sized B2 phase particles act as the apparent preferential sites for corrosion, inducing the dissolution of BCC phase and formation of corrosion pits. Obviously, the selective corrosion of BCC phase indicates the weak regions where BCC phase located facilitates the initiation and development of localized corrosion. In fact, the corrosion performance of HEAs depends on the protective effect of passive film and the occurrence of corrosion indicates that the passive film has been damaged [41]. The corrosion resistance of different phase is inextricably associated with the composition and structure of the passive film on its surface [16]. As reported in the related research [16, 42, 43], the Cr substances are beneficial to improve the stability and protection of the film, while the Al species easily reduce the compactness and protection of the passive film. The enriched element of different phases would lead to the composition difference of surface oxide film, affecting the stability and protection of passive films formed on the different phases. The formation of dense and protective film on the Cr-rich phase can be attributed to the existence of Cr oxide/hydroxide. In contrast, the passive film with decreased protective ability and inhomogeneity form on Al-rich phase due to the formation of Al substance. So the Al-rich B2 phase is more susceptible to corrosion because the relatively weak

Fig. 7 SEM images of the $Al_{0.3}Co_xCrFeNi$ HEA after potentiodynamic polarization in the 3.5 wt% NaCl solution at room temperature: (a–c) $Co_{0.25}$, (d–f) $Co_{0.5}$ and (g–i) $Co_{1.0}$

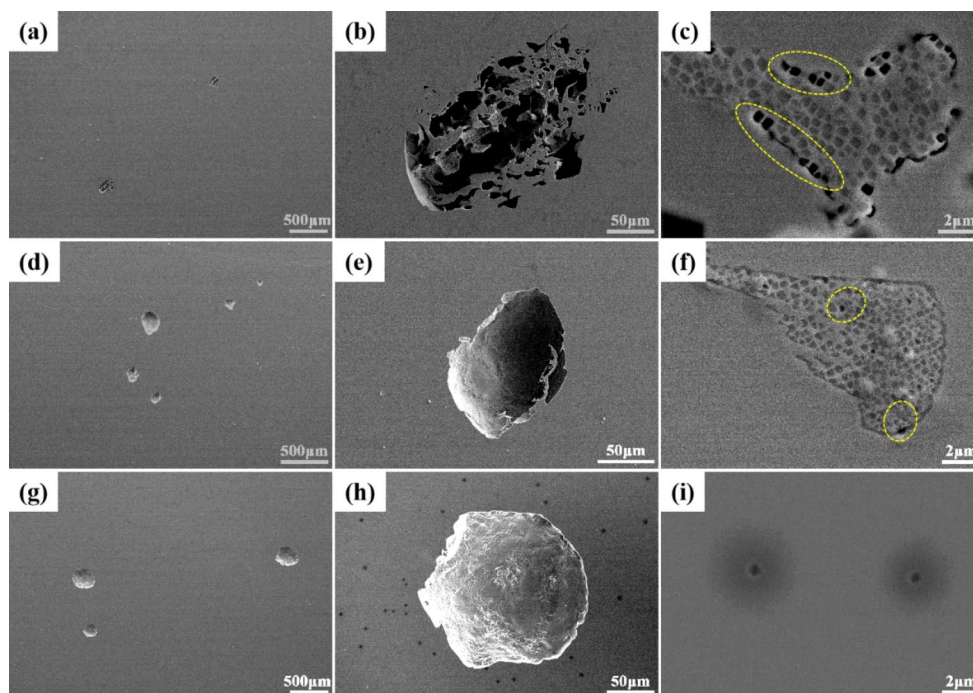


Fig. 8 EBSD analysis of the $\text{Co}_{0.25}$ alloy: (a) IPF image, (b) phase map and (c) KAM diagram

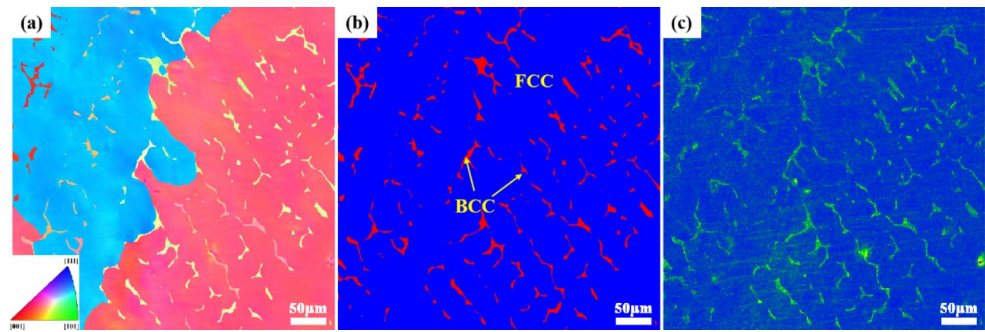
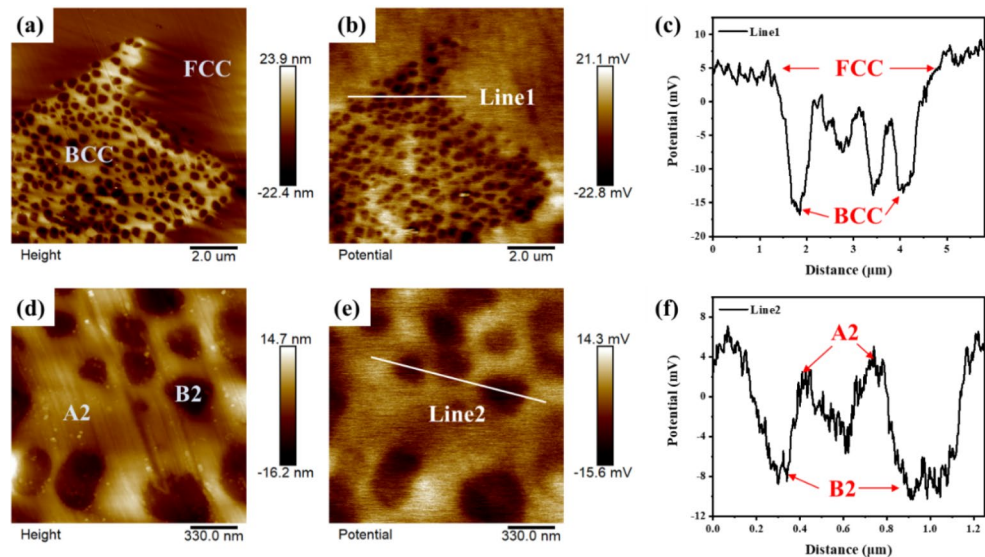


Fig. 9 The results of SKPFM measurements of the $\text{Co}_{0.25}$ alloy: (a, d) surface morphology images, (b, e) surface potential diagrams and (c, f) Potential profile of the line represented in the potential map



protective film is more likely to preferential breakdown, and the Cr-rich A2 phase shows better corrosion resistance than Al-rich B2 phase due to the passive film with stronger protection effect. Similarly, the oxide film formed on the BCC phase is Al-rich, Cr-depleted, and less protective than that of the FCC phase. Thus, the BCC phase rich in Al is more prone to corrosion compared to the FCC phase rich in Cr. So the $\text{Co}_{0.25}$ alloy with significantly higher proportion of BCC phase shows more inferior corrosion resistance due to more locations where localized corrosion occur. With the content of Co increase, the proportion of BCC phase decreases, leading to the possibility of localized corrosion reduces and the corrosion resistance is improved.

Figure 8 shows the EBSD results including IPF image, phase map, and kernel average misorientation (KAM) diagram of $\text{Co}_{0.25}$ alloy with duplex phase. The staggered distribution with typical dendrite structure of BCC phase and FCC phase has been described in Fig. 2. In general, KAM diagram is used to preliminarily analyze the distribution of lattice defects (dislocations, distortion etc.), in which the blue color represents the regions with lower defect density, the green color represents the regions with higher defect density [44]. It is clearly seen that the KAM value in BCC phase is extensively higher than that in FCC phase, which

implies that high defect density exists in the region of BCC phase compared to the FCC phase. The BCC phase with relatively high defect density indicates high energy storage inside this region, which illustrates the higher electrochemical reactivity and larger corrosion driving force of BCC phase in the corrosion process [45].

Furthermore, SKPFM measurements are performed to explain the selective corrosion of the double-phase HEAs. According to surface morphology images, the FCC phase and BCC phase with nanoscale porous structure in Fig. 9a, the B2 phase nano-particles (dark) and net-like A2 phase (light) in Fig. 9d can be easily distinguished. As shown in Fig. 9b, it can be observed that the potential of FCC phase is higher than that of BCC phase. The result of potential line scan (Fig. 9c) shows the potential difference is about 20 mV higher at the different phase. Comparing the potential of the B2 phase and A2 phase (Fig. 9e), the bright regions of potential refer to the A2 phase and the dark regions correspond to the B2 phase. The potential difference with about 15 mV shown in Fig. 9f also confirms the existence of lower potential of B2 phase. It is widely acknowledged that the phases with higher potential act as cathode, which could induce the preferential corrosion of the surrounding substrates in the corrosion process [14, 44]. The galvanic effect of different

phases driven by the distinction of potential accelerate the localized corrosion. Therefore, it can be clearly concluded that the BCC phase is more prone to corrosion compared to FCC phase and the B2 phase in BCC phase preferentially dissolve, which is consistent with the corrosion phenomenon in Fig. 7. It can be concluded that the influence of Co content on corrosion behavior of $\text{Al}_{0.3}\text{Co}_x\text{CrFeNi}$ ($x=0.25, 0.5$ and 1.0) HEAs can be attributed to the phase evolution and variation of elemental distribution caused by the adjustment of Co content.

Following the results presented and discussion above, it is found that pitting corrosion randomly occurs on the surface of HEAs with single FCC phase, and the corrosion mechanism is relatively simple that will not be further analyzed. Figure 10 shows the schematic diagram of the corrosion mechanism for the double-phase HEAs. In the corrosive environment, a passive film with protective effect is formed on the surface of HEAs, and the obvious differences exist in corrosion resistance of different regions due to the distinction in phase components. Overall, the protective film at BCC phase is priority to be damaged and localized corrosion occurs. At the initial stage of corrosion, pitting corrosion occurs preferentially at B2 phase because of the less protective passive film formed on the surface (Fig. 10b). Subsequently, B2 phase dissolves continuously to form pits under the galvanic effect between B2 and A2 phases (Fig. 10c). With the further development of corrosion, the A2 matrix also begins to corrode and the alloy shows the

selective corrosion of BCC phase due to the lower potential compared to the FCC phase (Fig. 10d). Finally, as shown in Fig. 10e, the BCC phase is completely dissolved to form corrosion pits with large depth, and the corrosion of FCC phase appears. Meanwhile, the constituent elements dissolved in the solution combine with OH^- to form corrosion products (metallic oxides and hydroxides) accumulating on the surface.

4 Conclusion

In this work, the effect of Co content on the microstructure evolution and corrosion behavior of $\text{Al}_{0.3}\text{Co}_x\text{CrFeNi}$ HEAs were investigated. The mixed phase of FCC + BCC of $\text{Co}_{0.25}$ and $\text{Co}_{0.5}$ alloys transforms into single FCC structure of $\text{Co}_{1.0}$ alloy with the increase of Co content, and the BCC phase consists of (Al, Ni)-rich nano-sized particles B2 phase and (Cr, Fe, Co)-rich net-like A2 phase. The lower potential and relatively weak passive films on surface make the B2 phase into the positions of preferential localized corrosion. Similarly, the BCC phase act as anode that is more prone to corrosion compared to the FCC phase. In addition, the higher dislocation density at BCC phase could also contribute to the acceleration of the localized corrosion. The $\text{Co}_{0.25}$ and $\text{Co}_{1.0}$ alloys suffer from selective corrosion at the regions where BCC phase located while pitting corrosion occurs on the $\text{Co}_{1.0}$ alloy. Therefore, the increase of

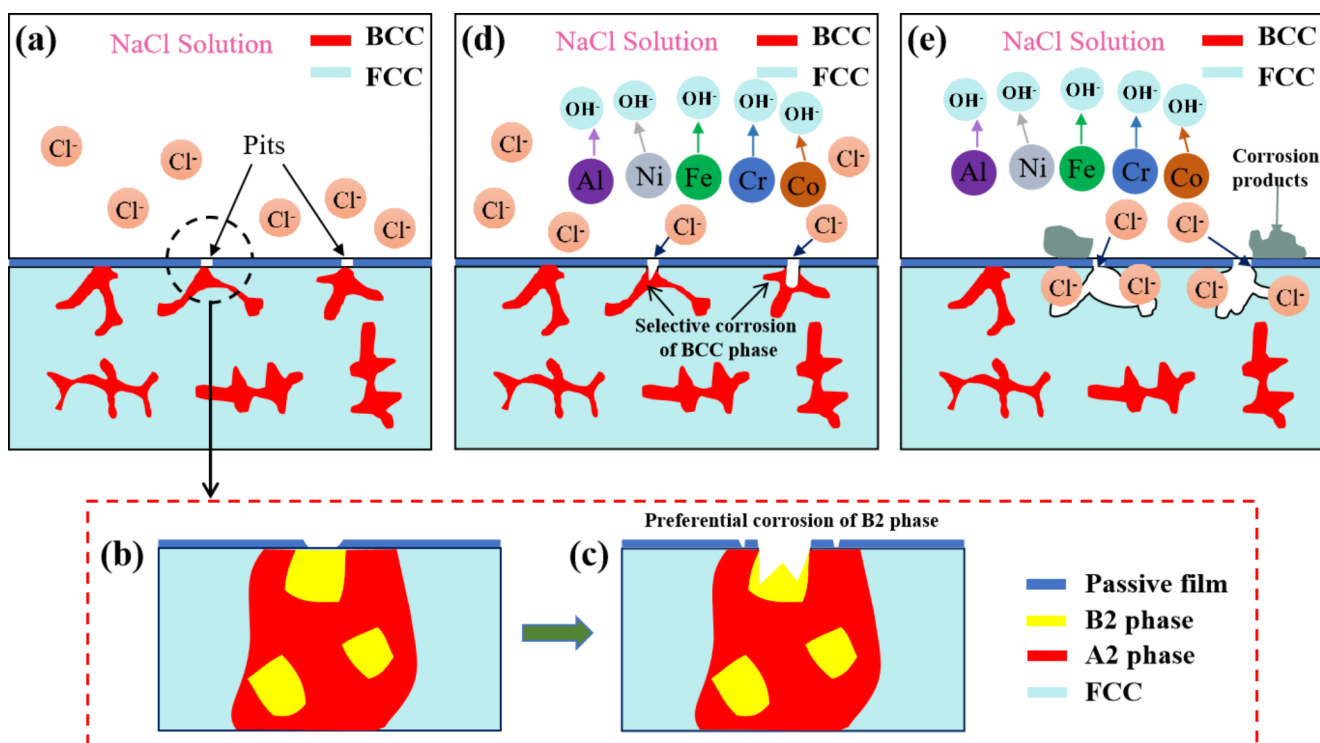


Fig. 10 Schematic diagram of the corrosion mechanism for the double-phase HEAs.

Co content is conducive to reduce the proportion of BCC phase, thus effectively improving the corrosion resistance of HEAs.

Acknowledgements This work was supported by the National Natural Science Foundation of China (Grant No. 51901018), Young Elite Scientists Sponsorship Program by China Association for Science and Technology (YESS, 2019QNRC001), the Fundamental Research Funds for the Central Universities (Grant No. FRF-AT-20-07, 06500119), the Natural Science Foundation of Beijing Municipality (Grant No. 2212037), the National Science and Technology Resources Investigation Program of China (Grant No. 2019FY101400).

Data and code Availability The raw/processed data required to reproduce these findings cannot be shared at this time as this data also forms part of an ongoing study.

Declarations

CRedit Authorship Contribution Statement Zequn Zhang: Conceptualization, Data curation, Writing-original draft preparation, Formal analysis. Qijuan Dong and Zhibin Chen: Data curation, Formal analysis, Simulation. Junsheng Wu: Supervision. Jiuyang Xia and Kang Huang: Project administration, validation. Pengcheng Zuo and Wei Xue: Formal analysis. Bowei Zhang: Writing-reviewing and editing.

Conflict of Interest or Competing Interests The authors declare that they have no known competing financial interests or personal relationships that could have appeared to influence the work reported in this paper.

References

1. Y. Zhang, T.T. Zuo, Z. Tang, M.C. Gao, K.A. Dahmen, P.K. Liaw, Z.P. Lu, *Prog. Mater. Sci.* **61**, 1–93 (2014). <https://doi.org/10.1016/j.pmatsci.2013.10.001>
2. M.-H. Tsai, J.-W. Yeh, *Mater. Res. Lett.* **2**, 107–123 (2014). <https://doi.org/10.1080/21663831.2014.912690>
3. D.B. Miracle, O.N. Senkov, *Acta Mater.* **122**, 448–511 (2017). <https://doi.org/10.1016/j.actamat.2016.08.081>
4. J.-W. Yeh, S.-K. Chen, S.-J. Lin, J.-Y. Gan, T.-S. Chin, T.-T. Shun, C.-H. Tsau, S.-Y. Chang, *Adv. Eng. Mater.* **6**, 299–303 (2004). <https://doi.org/10.1002/adem.200300567>
5. Y. Fu, J. Li, H. Luo, C.W. Du, X.G. Li, *J. Mater. Sci. Technol.* **80**, 217–233 (2021). <https://doi.org/10.1016/j.jmst.2020.11.044>
6. Z. Li, K.G. Pradeep, Y. Deng, D. Raabe, C.C. Tasan, *Nature* **534**, 227–230 (2016). <https://doi.org/10.1038/nature17981>
7. E.P. George, W.A. Curtin, C.C. Tasan, *Acta Mater.* **188**, 435–474 (2020). <https://doi.org/10.1016/j.actamat.2019.12.015>
8. Y. Liang, L. Wang, Y. Wen, B. Cheng, Q. Wu, T. Cao, Q. Xiao, Y. Xue, G. Sha, Y. Wang, Y. Ren, X. Li, L. Wang, F. Wang, H. Cai, *Nat. Commun.* **9**, 4063 (2018). <https://doi.org/10.1038/s41467-018-06600-8>
9. N. Hua, W. Wang, Q. Wang, Y. Ye, S. Lin, L. Zhang, Q. Guo, J. Brechtel, P.K. Liaw, *J. Alloys Compd.* **861**, 157997 (2021). <https://doi.org/10.1016/j.jallcom.2020.157997>
10. H. Ju, K. Huang, J. Luan, Y. Geng, J. Yang, J. Xu, *Ceram. Int.* **49**, 30115–30124 (2023). <https://doi.org/10.1016/j.ceramint.2023.06.267>
11. Y. Shi, B. Yang, P.K. Liaw, *Metals* **7**, 43 (2017). <https://doi.org/10.3390/met7020043>
12. N. Kumar, M. Fusco, M. Komarasamy, R.S. Mishra, M. Bourham, K.L. Murty, *J. Nucl. Mater.* **495**, 154–163 (2017). <https://doi.org/10.1016/j.jnucmat.2017.08.015>
13. H. Luo, Z. Li, A.M. Mingers, D. Raabe, *Corros. Sci.* **134**, 131–139 (2018). <https://doi.org/10.1016/j.corsci.2018.02.031>
14. Y. Shi, L. Collins, N. Balke, P.K. Liaw, B. Yang, *Appl. Surf. Sci.* **439**, 533–544 (2018). <https://doi.org/10.1016/j.apsusc.2018.01.047>
15. Y. Fu, C. Dai, H. Luo, D. Li, C. Du, X. Li, *Appl. Surf. Sci.* **560**, 149854 (2021). <https://doi.org/10.1016/j.apsusc.2021.149854>
16. Z. Wang, G.H. Zhang, X.H. Fan, J. Jin, L. Zhang, Y.X. Du, *J. Alloys Compd.* **900**, 163432 (2022). <https://doi.org/10.1016/j.jallcom.2021.163432>
17. C.B. Nascimento, U. Donatus, C.T. Ríos, R.A. Antunes, *Mater. Chem. Phys.* **267**, 124582 (2021). <https://doi.org/10.1016/j.matchemphys.2021.124582>
18. C.C. Yen, H.N. Lu, M.H. Tsai, B.W. Wu, Y.C. Lo, C.C. Wang, S.Y. Chang, S.K. Yen, *Corros. Sci.* **157**, 462–471 (2019). <https://doi.org/10.1016/j.corsci.2019.06.024>
19. S. Wang, Y. Zhao, X. Xu, P. Cheng, H. Hou, *Mater. Chem. Phys.* **244**, 122700 (2020). <https://doi.org/10.1016/j.matchemphys.2020.122700>
20. C.M. Lin, H.L. Tsai, *Intermetallics* **19**, 288–294 (2011). <https://doi.org/10.1016/j.jallcom.2020.157712>
21. Y. Wang, J. Jin, M. Zhang, X. Wang, P. Gong, J. Zhang, J. Liu, *J. Alloys Compd.* **858**, 157712 (2021). <https://doi.org/10.1016/j.jallcom.2020.157712>
22. A. Parakh, M. Vaidya, N. Kumar, R. Chetty, B.S. Murty, *J. Alloys Compd.* **863**, 158056 (2021). <https://doi.org/10.1016/j.jallcom.2020.158056>
23. A. Munitz, S. Salhov, S. Hayun, N. Frage, *J. Alloys Compd.* **683**, 221–230 (2016). <https://doi.org/10.1016/j.jallcom.2016.05.034>
24. Y. Yu, P. Shi, K. Feng, J. Liu, J. Cheng, Z. Qiao, J. Yang, J. Li, W. Liu, *Acta Metall. Sin.* **33**, 1077–1090 (2020). <https://doi.org/10.1007/s40195-020-01002-6>
25. H.P. Chou, Y.S. Chang, S.K. Chen, J.W. Yeh, *Mater. Sci. Eng. B* **163**, 184–189 (2009). <https://doi.org/10.1016/j.mseb.2009.05.024>
26. M.C. Oh, A. Sharma, H. Lee, B. Ahn, *Intermetallics* **139**, 107369 (2021). <https://doi.org/10.1016/j.intermet.2021.107369>
27. Y. Shi, B. Yang, X. Xie, J. Brechtel, K.A. Dahmen, P.K. Liaw, *Corros. Sci.* **119**, 33–45 (2017). <https://doi.org/10.1016/j.corsci.2017.02.019>
28. Q. Dong, W. Jia, Z. Zhang, D. Zhang, J. Wu, B. Zhang, *Mater. Corros.* **73**, 1274–1285 (2022). <https://doi.org/10.1002/maco.202112851>
29. G. Qin, W. Xue, C. Fan, R. Chen, L. Wang, Y. Su, H. Ding, J. Guo, *Mater. Sci. Eng. A* **710**, 200–205 (2018). <https://doi.org/10.1016/j.msea.2017.10.088>
30. S. Kumar, A. Patnaik, A.K. Pradhan, V. Kumar, *J. Mater. Eng. Perform.* **28**, 4111–4119 (2019). <https://doi.org/10.1007/s11665-019-04162-4>
31. X.W. Qiu, M.J. Wu, C.G. Liu, Y.P. Zhang, C.X. Huang, *J. Alloys Compd.* **708**, 353–357 (2017). <https://doi.org/10.1016/j.jallcom.2017.03.054>
32. Z. Zhang, J. Sun, J. Xia, J. Wu, Z. Chen, B. Zhang, Z. Li, X. Li, B. Zhang, *Corros. Sci.* **208**, 110634 (2022). <https://doi.org/10.1016/j.corsci.2022.110634>
33. C. Liu, X. Li, R.I. Revilla, T. Sun, J. Zhao, D. Zhang, S. Yang, Z. Liu, X. Cheng, H. Terryn, X. Li, *Corros. Sci.* **179**, 109150 (2021). <https://doi.org/10.1016/j.corsci.2020.109150>
34. M. Li, L. Guo, L. Qiao, Y. Bai, *Corros. Sci.* **60**, 76–81 (2012). <https://doi.org/10.1016/j.corsci.2012.04.010>
35. B. Sun, Z. Liu, Y. He, F. Cao, X. Li, *Corros. Sci.* **187**, 109505 (2021). <https://doi.org/10.1016/j.corsci.2021.109505>
36. S. Kumar, A. Patnaik, A.K. Pradhan, V. Kumar, *J. Mater. Res.* **34**, 841–853 (2019). <https://doi.org/10.1557/jmr.2018.499>

37. S. Guo, C. Ng, J. Lu, C.T. Liu, J. Appl. Phys. **109**, 103505 (2011). <https://doi.org/10.1063/1.3587228>
38. W.R. Wang, W.L. Wang, J.W. Yeh, J. Alloys Compd. **589**, 143–152 (2014). <https://doi.org/10.1016/j.jallcom.2013.11.084>
39. Y. Shi, L. Collins, R. Feng, C. Zhang, N. Balke, P.K. Liaw, B. Yang, Corros. Sci. **133**, 120–131 (2018). <https://doi.org/10.1016/j.corsci.2018.01.030>
40. M. Aizenshtein, S. Hayun, Metallogr. Microstruct. Anal. **9**, 305–311 (2020). <https://doi.org/10.1007/s13632-020-00643-4>
41. Q. Zhao, Z. Pan, X. Wang, H. Luo, Y. Liu, X. Li, Corros. Sci. **208**, 110666 (2022). <https://doi.org/10.1016/j.corsci.2022.110666>
42. X. Yan, H. Guo, W. Yang, S. Pang, Q. Wang, Y. Liu, P.K. Liaw, T. Zhang, J. Alloys Compd. **860**, 158436 (2021). <https://doi.org/10.1016/j.jallcom.2020.158436>
43. C. Dai, T. Zhao, C. Du, Z. Liu, D. Zhang, J. Mater. Sci. Technol. **46**, 64–73 (2020). <https://doi.org/10.1016/j.jmst.2019.10.020>
44. Y. Shi, B. Yang, P.D. Rack, S. Guo, P.K. Liaw, Y. Zhao, Mater. Des. **195**, 109018 (2020). <https://doi.org/10.1016/j.matdes.2020.109018>
45. C.B. Nascimento, U. Donatus, C.T. Ríos, R.A. Antunes, J. Mater. Res. Technol. **9**, 13879–13892 (2020). <https://doi.org/10.1016/j.jmrt.2020.10.002>

Publisher's Note Springer Nature remains neutral with regard to jurisdictional claims in published maps and institutional affiliations.

Springer Nature or its licensor (e.g. a society or other partner) holds exclusive rights to this article under a publishing agreement with the author(s) or other rightsholder(s); author self-archiving of the accepted manuscript version of this article is solely governed by the terms of such publishing agreement and applicable law.